Nanoplasma resonance condition in the middle-infrared spectral range

V. Leshchenko, B. Smith, A. Camacho Garibay, P. Agostini, L. Fang, and L. F. DiMauro

Phys. Rev. E **107**, 055207 — Published 12 May 2023

DOI: 10.1103/PhysRevE.107.055207

Nano-plasma resonance condition in the middle-infrared spectral range

V. Leshchenko*
Department of Physics, The Ohio State University, Columbus, Ohio 43210, USA and
NeXUS facility, Institute for Optical Science, The Ohio State University, Columbus, Ohio 43210, USA

B. Smith, A. Camacho Garibay, P. Agostini, and L.F. DiMauro
Department of Physics, The Ohio State University, Columbus, Ohio 43210, USA

L. Fang
Department of Physics, The Ohio State University, Columbus, Ohio 43210, USA and
Department of Physics, University of Central Florida, Orlando, Florida 32816, USA

The resonance-absorption condition in the laser-nano-plasma interactions has been considered to follow the wavelength dependence of the critical plasma density. We experimentally demonstrate that this assumption fails in the middle-infrared spectral range, while it is valid for visible and near-infrared wavelengths. A thorough analysis supported by molecular dynamic (MD) simulations indicate that the observed transition in the resonance condition is caused by the reduction of the electron scattering rate and the associated increase of the cluster outer-ionization contribution. A new expression for the nano-plasma resonance density is derived based on experimental results and MD-simulations. The findings are important for a broad range of plasma experiments and applications, since the extension of the laser-plasma interaction studies to longer wavelengths has become increasingly topical.

INTRODUCTION

Direct in-situ measurement of plasma parameters is crucial for many studies and applications [1, 2]. While there is a well established set of diagnostics tools for macroscopic plasmas [1, 3, 4], diagnostics of nano-plasmas is more challenging. Due to the nanometer scale, nano-plasmas inherently demonstrate ultrafast dynamics that often involves non-equilibrium transitions [5], which are difficult to measure. Many plasma diagnostics and applications rely on resonant absorption of laser radiation by plasmas, which is typically defined by the critical plasma density [6]

$$n_c = m_e \pi c^2 / e^2 \lambda_{pr}^2, \qquad (1)$$

or proportional to it, as in the case of the surface plasmon (Mie) resonance [7], where λ_{pr} is the wavelength of the probe laser field; m_e and e are the electron's mass and charge, respectively. Here we experimentally show that the nano-plasma density corresponding to the resonance absorption condition deviates from the n_c scaling in the short-wave infrared (SWIR) spectral range, while it indeed follows n_c scaling in the visible and near-infrared (NIR) ranges.

Although a number of important studies of laser-nano-plasma interactions have been done in the last few decades, almost all time-resolved (pump-probe) studies are limited to ∼800 nm wavelength for both pump and probe pulses. These studies include: time-resolved interferometry measuring the complex electric susceptibility of a cluster beam [8], ion-charge-resolved [9–11] and absorption experiments [12], delay-dependent measurements of ion/electron kinetic energy [13, 14]. In addition, there are a couple of diffraction experiments performed at free-electron lasers (FEL) [15, 16] with 800 nm pump pulses. These works have made a number of significant contributions: (i) identifying that there is a clear resonance delay with enhancement of the measured parameters; (ii) this resonance is very broad and smeared compared to uniform-density simulations, which is attributed to inhomogeneous plasma density; (iii) the radially inhomogeneous density of expanding nano-plasmas was directly confirmed in the FEL diffraction experiments; (iv) the resonance position shifts to longer delays for larger cluster sizes (almost linearly) and to shorter delays for higher pump intensities.

The growing interest of the laser-plasma community to SWIR and long-wave infrared (LWIR) optical drivers [17–19] and rapidly increasing capabilities of laser systems in these spectral ranges [20] require the extension of fundamental plasma studies to longer wavelengths. Here we extend time resolved nano-plasma studies to wavelengths significantly longer than 800 nm, covering a considerable portion of the SWIR range. We find a fundamental change of the condition of resonant absorption of optical pulses by nano-plasmas that could not be identified in fixed-wavelength studies. A comparison with Molecular Dynamics (MD) simulations reveals that the origin is a fundamental change in the plasma heating mechanism at different densities, which modifies the plasma resonance conditions for probe pulses of different wavelengths. This finding has general importance for laser-plasma applications and diagnostics especially at surfaces where the plasma density profile is a pivotal element or critical control parameter, a few examples are: generation of coherent soft-X-rays through surface high-harmonic generation (plasma mirror) [21, 22], monoenergetic ion beam generation [23], generation of X-rays and energetic charged particles [24–27], pulse cleaning via transient plasma mirrors [28].

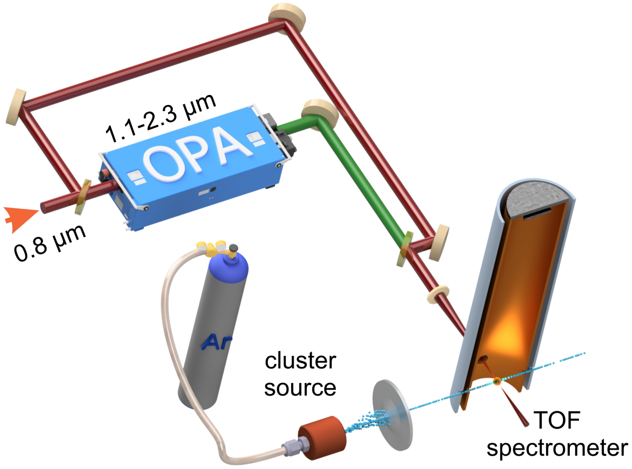

FIG. 1. Scheme of the experimental setup. The output of a Ti:Sapphire laser is split into two parts: one is used to create nano-plasmas by ionizing argon clusters, another generates tunable probe pulses in an OPA. Clusters are skimmed before entering the interaction area where they are ionized by the optical beams, and the kinetic energy of the generated ions is detected with a TOF spectrometer.

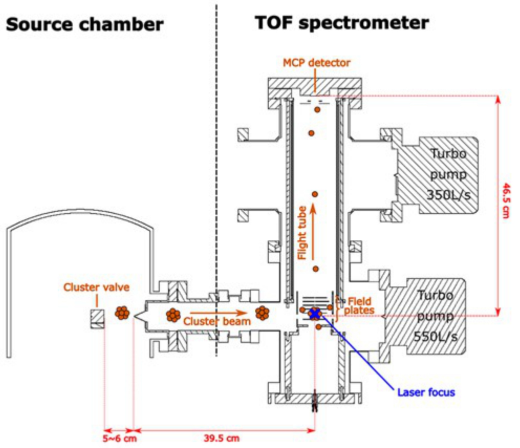

FIG. 2. Sketch of the experimental vacuum chambers.

EXPERIMENTAL SETUP

The experiment is performed with a home-built Ti:Sapphire laser system delivering 800 nm pulses with 60 fs duration, 5.6 mJ energy at 1 kHz repetition rate. The scheme of the experiment in shown in Fig. 1. About 90% of the power is used to pump an optical parametric amplifier (OPA) (HE-TOPAS, Light Conversion), the remaining 10% is used as a pump pulse in pump-probe configuration. The OPA output is tunable in the range between 1.15 µm and 2.3 µm; in addition, the second harmonic generation is utilized to extend the probe range down to 0.6 µm. The nano-plasmas are generated by laser-induced ionization of argon van der Waals nano-clusters. The cluster beam is produced with a pulsed gas nozzle and skimmed before entering the interaction area where clusters are ionized by the optical beams, and the kinetic energy of the generated ions is detected with a time of flight (TOF) spectrometer.

Cluster source

The scheme of the vacuum part of the experimental setup is presented in Fig. 2. The cluster beam is produced with a solenoid-driven (Even-Lavie [29]) pulsed gas nozzle with 150 μm diameter, 28 μs opening time, and 30 bar argon backing pressure. The nozzle position is controlled with a 3-dimensional translation stage. The translation stage enables alignment of the cluster beam to the molecular beam skimmer (Beam Dynamics Inc.) with a 1 mm diameter. The nozzle is mounted in a water/ice cooled copper holder maintaining about 5 C temperature to ensure stable and reproducible clustering conditions and the corresponding cluster size. The temperature of the nozzle is monitored with an in-vacuum thermocouple.

All experiments presented in the paper are performed at 500 Hz, which is the maximum operation frequency of the solenoid valve. The cluster source chamber and the interaction chamber are separated by a skimmer that serves two purposes: differential pumping and selecting the central part of the cluster beam with highest density and largest cluster sizes. Ions generated by the nano-plasma explosions triggered by the laser-induced ionization are detected in a time of flight (TOF) spectrometer with a micro-channel plate (MCP) detector at the the flight tube length of 46.5 cm.

The size of generated clusters is experimentally measured with a combination of Rayleigh scattering and interferometry [30, 31]. Interferometry was implemented with 800 nm linearly polarized laser beam by imaging the nozzle output on a CCD camera. Rayleigh scattering was measured with 400 nm pulses, which are the second harmonic of the pump laser (generated in a 200 µm thick beta-barium borate (BBO) crystal). Scattered light from the cluster jet is collected at 90 degrees relative to the plain containing the cluster beam and the 400 nm beam using a vacuum compatible fiber. The collected scattered light is extracted from the vacuum through a UHV fiber feedthrough and recorded with a photomultiplier tube (PMT) R282 (Hamamatsu).

The measured averaged cluster size is 7±0.5 nm (for details on the reconstruction procedure see [31]; g parameter of 0.15 was used). The measured cluster size is close to the estimate based on the Hagena parameter [31], which predicts the size of 9 nm for our experimental conditions. The direct measurement of the cluster size distribution was not possible in our setup, but from the previous publications with similar experimental conditions it should be Gaussian (see [31] and references in it) so that $(\langle N^2\rangle - \langle N\rangle^2)/\langle N\rangle^2 \approx 0.2$, where N is the number of atoms per cluster.

The diameter of the cluster beam in the interaction region is about 1.5 mm as identified during the adjustment of the spatial overlap between the focus of the optical beam and the cluster beam. The estimated density of the clusters in the interaction volume is about 10^9 clusters×cm^{-3} (the corresponding averaged atomic density is 3×10^{13} cm^{-3}).

Optical setup

Pump and probe optical pulses are collinearly combined with a dichroic mirror (PN86-079, EdmundOptics) and focused with a plano-convex uncoated CaF_2 lens with 10 cm focal length through an uncoated CaF_2 window with 2 mm thickness. The lens is mounted on a 3-dimensional translation stage, and the position of the focus is aligned to the center of the cluster beam by maximizing the yield of ions. The diameter of the pump beam on the lens was about 3 mm, which corresponds to f-number (F/D) of 33. The OPA beam was about twice larger to ensure about the same focused diameter. A 1:1.25 telescope is used in the probe-beam arm to adjust divergence and overlap the waist of the probe beam with the waist of the pump beam (as the focal length of a lens depends on the wavelength due to dispersion). The spatial and temporal overlap between the beams was adjusted *in situ* by maximizing the electron yield from ionization of atomic argon, which was introduced in the chamber with a leak valve during the alignment (to facilitate the alignment, a pre-alignment was done in air using sum frequency generation in a BBO crystal). It is an extremely precise and sensitive technique due to a highly nonlinear dependence of the ionization rate on the strength of the electric field [32].

The intensity of the pump and probe pulses was determined in-situ by analyzing the 2Up and 10Up classical cutoffs present in the photoelectron energy distribution from strong field ionization [33] of atomic neon for shorter wavelengths and argon for longer wavelengths. It was also verified to be very close to the values expected from the measurement of spatial and temporal pulse profiles; where the spatial profile was measured with a CCD camera, and the temporal pulse shape was determined with a second-harmonic generation frequency-resolved optical gating (SHG-FROG) setup.

THEORETICAL MODEL

MD simulations were performed to support the explanation of our experimental findings. The system initial geometry is obtained by constructing a three-dimensional array of atoms following an icosahedral geometry. The minimum interatomic distance in this geometry is scaled to the corresponding atomic Van der Waals diameter of 7.1 a.u. for Argon, and the whole system is inscribed inside a sphere of the cluster radius (R_{cl}). In order to obtain a converging energy spectra with statistical significance, calculations for several cluster orientations are performed by rotating the initial distribution of atoms by random angles along randomly chosen axes. Additionally, every particle is randomly shifted (by less than 0.5 a.u. in any coordinate with equal probability for the ions, and less than 0.1 a.u. for the electrons). Time evolution is entirely classical, as electrons and ions are considered to be point particles that are propagated following Newton's equations of motion. Electron-electron and ion-ion interactions are calculated according to the Coulomb potential, while the interaction between an electron i and an ion j is accounted through the use of a soft-core potential of the form

$$V_{ij}(r_i, R_j) = -\frac{q_j}{\sqrt{|r_i - R_j|^2 + \alpha^2}}. \tag{2}$$

This potential removes the singularity of the Coulomb interaction and provides numerical stability. The system so obtained is essentially in equilibrium in its initial condition, as the constituting particles are almost non-interacting save for some residual weak dipole-dipole interactions. In fact, when allowed to propagate freely, the integrity of the system is preserved for tens of picoseconds.

The soft-core parameter α is chosen such that the maximum electric field experienced by an electron in this potential coincides with the over the barrier ionization condition (namely $E_{OBI} = I_p^2/4$) as follows

$$\alpha = \sqrt{\frac{8}{3\sqrt{3}}\frac{1}{I_p}}, \tag{3}$$

which in the case of Argon is $\alpha = 2.142$, mimicking in this way ionization conditions in Coulomb potentials. It should be noticed that the choice of the parameter α is not unique and it will depend on the particular application and ionization mechanism. For example, when applied to the XUV regime, α is often chosen such that the minimum of the potential well corresponds with the ionization energy [34].

An ionization event is considered to have taken place when an electron leaves the vicinity of its parent ion (according to $r > r_{VW}$). When such an event is detected, the charge of the parent ion is increased by one unit, the distance of the ionized electron is no longer tracked, and a new electron is added to the calculation at the bottom of the atom's updated potential. This allows us to add particles to the simulation scheme smoothly and without introducing abrupt changes in the propagation, while keeping the computation only as expensive as absolutely needed.

Soft-core potentials have an important physical flaw, which is its inability to produce large angle scattering. This collision mechanism is fundamental for the production of energetic ions as well as inverse Bremmstrahlung heating, and thus cannot be neglected. This issue is addressed by noticing that the smoothing parameter α itself defines a region $r_{ij} < r_{SC}$ where the Coulomb potential is neglected. We can compensate this flaw by considering that any electron entering this region whose kinetic energy is larger than the binding energy can be propagated along a collisional trajectory according to Keplers law. This particular propagation scheme has been

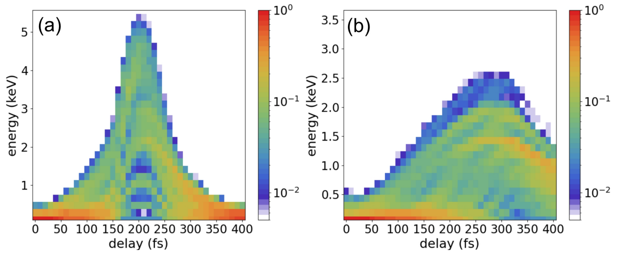

FIG. 3. Ion energy distribution in MD-simulations of the laser-cluster interaction. Examples of pump-probe scans for probe wavelengths of 0.9 µm **(a)** and 2.5 µm **(b)** are shown. In both cases the pump pulse has 800 nm central wavelength, 60 fs FWHM pulse duration, and 200 TW/cm^2 peak intensity; the probe intensity is 100 TW/cm^2; the probe pulse duration is 60 fs.

used to successfully simulate electron energy spectra of clusters under strong fields [35]. In this way, all the interactions relevant to the plasma dynamics and energy absorption are included, without the need to explicitly introduce additional parameters such as interaction cross-sections or heating rates.

Each laser pulse has Gaussian temporal shape, and the calculation is performed in the dipole approximation such that the electric field is homogeneous over the whole system. While the homogeneity of the laser field makes for a vanishing magnetic field, other effects such as screening or field enhancement are implicitly included due to the particle response to the pulse.

A couple examples of a MD-simulation scans for the initial cluster radius of 2 nm are shown in Fig. 3.

EXPERIMENTAL RESULTS

Resonance in pump-probe scans

A couple of typical pump-probe scans are shown in Fig. 4. In both a 2D scan (a, b) and a mean energy plot (c, d), one can see a clear maximum in the detected ion energy, which corresponds to resonant absorption conditions of the probe pulse by the nano-plasma. Unlike in simplified models [7] with homogeneous plasma density, the measured resonance is quite broad, which agrees with all other nano-plasma pump-probe experiments known to us [8–14]. The width has two main contribution: one is the inhomogeneous plasma density, which result in different resonance delay for different plasma shells; another is the natural width of the plasma resonance itself, see e.g. Fig. 5 in [7].

In order to quantify the resonance delay, the ion mean kinetic energy (examples are shown in Fig. 4(c, d)) is fitted with a modified Maxwellian function:

$$K(t) = \frac{A}{C}(t-T_0)^B \exp\left(-\frac{(t-T_0)^2}{C^2}\right) + D, \tag{4}$$

where T_0 defines the resonance delay, and A, B, C, and D are the fitting parameters.

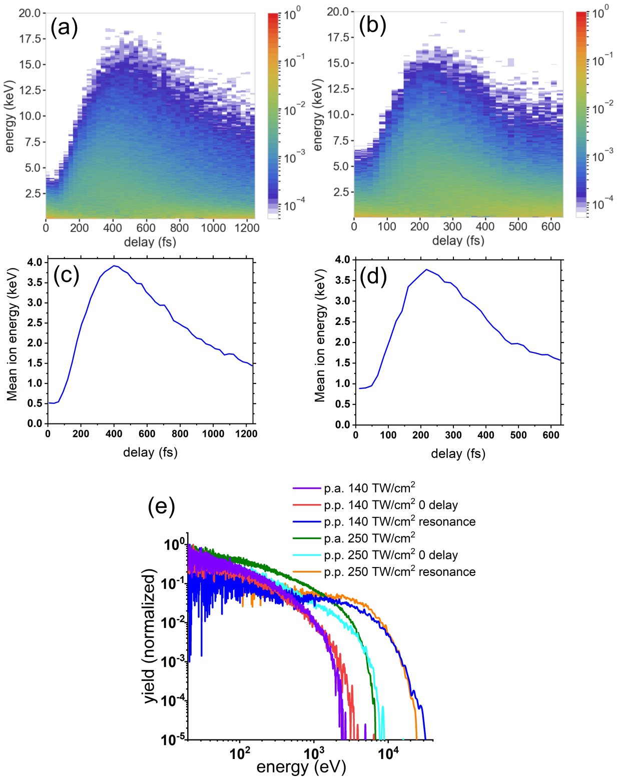

FIG. 4. **(a)** A typical scan of the ion kinetic energy distribution as a function of the pump-probe delay for 1.2 µm probe wavelength and 140 TW/cm^2 pump intensity. **(b)** Same but for 250 TW/cm^2 pump intensity. **(c-d)** Corresponding mean ion kinetic energy for 140 TW/cm^2 **(c)** and 250 TW/cm^2 **(d)**, which are used for the evaluation of the resonance position. **(e)** Examples of ion spectra. The pump-probe data are slices from (a) and (b) at corresponding delays. p.a. stands for pump alone; p.p. stands for the pump-probe case.

Note that the "background" from the pump pulse alone corresponds just to the vertical shift of the signal (e.g. in Fig. 4). It doesn't affect the precision of the measurement of the resonance delay, as it contributes only to the D parameter in the fit function and doesn't affect T_0, which is the only parameter that is used in the final data analysis. In addition, the background is relatively weak as can be seen in Fig. 4, since the signal at zero delay is 5–10 times weaker compared to the resonance.

Resonance plasma density

MD-simulations were used to identify plasma density corresponding to the observed resonance delay. Fig. 5(a) shows an MD simulation of the plasma density as a function of time for both pump-alone single-pulse case and the double-pulse case at the resonance delay of 200 fs for the 0.9 µm probe pulses. This example clearly shows that the resonance delay corresponds to the standard critical plasma density (Eq.1) for the pump-alone case (the orange solid line). The conclusion is clear by observing that orange and green lines intersect at the time equal to the resonance delay. This result agrees with previous simulations for 800 nm pulses [6]. In the pump-probe scenario, the plasma density reaches a local maximum of about $3n_c$ at the time equal to the resonance pump-probe delay. The increase of the density compared to the pump-alone case is caused by the ionization induced by the probe pulse. The height of the local maximum of $\sim 3n_c$ is defined by the outer-ionization. Outer-ionization is the scenario when a part of electrons is leaving the plasma, which acquires a positive net charge. In this process, the number of electrons in the nano-plasma is reducing as well as their temperature, since the fastest electrons are leaving the plasma; so the probability of collisional ionization substantially drops and the plasma density stops increasing. As identified in MD simulations (see Fig. 5(b)), outer-ionization is more efficient at densities $\sim 3n_c$, which defines the height of the local density maximum in the pump-probe case (Fig. 5(a)). Thus, addressing the long standing discussion of the nano-plasma resonance conditions, in experiments and realistic simulations allowing for inhomogeneous plasma density, the resonance plasma density is $n_c(\lambda_{pr})$ for probe wavelengths in visible and near-infrared ranges. However, higher density of about $3n_c$ is also important for outer-ionization, e.g. in pump-probe experiments where the probe is interacting with a pre-ionized cluster. Although $3n_c$ is in quantitative agreement with the widely accepted Mie resonance condition [7, 36], the nature is different compared to uniform-density theories like the nanoplasma model [7]. Namely, $3n_c$ is not the optimum density for plasma heating but the density when the heating is terminated by the nano-plasma outer-ionization.

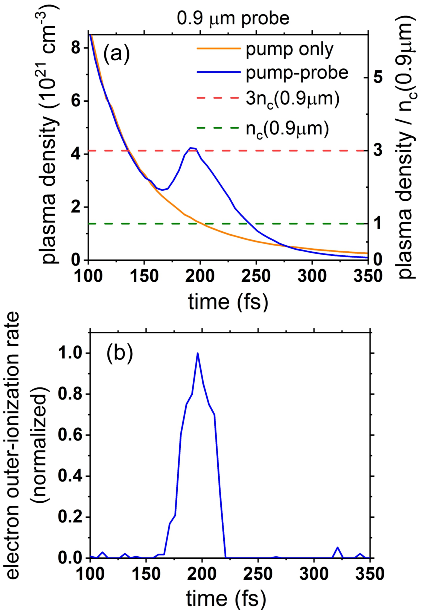

FIG. 5. MD simulation results for the probe wavelength of 0.9 μm and pump-probe delay of 200 fs, which is the resonance delay for this probe wavelength. **(a)** Temporal dependence of the plasma density. **(b)** Electron outer-ionization rate under the same conditions. Simulation parameters: the pump pulse has 0.8 μm central wavelength, 60 fs FWHM pulse duration, and 200 TW/cm^2 peak intensity; the probe pulse has 100 TW/cm^2 intensity and 60 fs duration. Time zero is the peak of the pump pulse.

Reconstruction of the plasma density dynamics

The measured dependence of the resonant delay on the probe wavelength and pump intensity is shown in Fig. 6(a). Higher pump intensities result in smaller resonant delays, which agrees with previous results discussed in the introduction. The resonant delay increases with the probe wavelength, following the general expectation based on the reduction of the critical plasma density n_c (Eq.1). A lower critical density results in a lower resonant density that is achieved at a later stage of plasma expansion. An important qualitative observation common for all scans is a "knee structure": a larger slope for shorter wavelengths and smaller at longer ones. It is even more clear in Fig. 6(b) where the plasma density is reconstructed from Fig. 6(a) by using the relation between the probe wavelength (λ_{pr}) and the critical plasma density Eq.1. In Fig. 6(b), all results have qualitatively identical behavior: there is a good agreement with simulations at plasma densities $> 5.7 \times 10^{20}$ cm^{-3} (corresponds to probe wavelengths <1.4 μm), while there is an increasing discrepancy at smaller densities (longer probe wavelengths).

Additionally, we test the assumption that the resonance condition occurs at n_c, solely relying on experimental results. In the following, we compare the ion kinetic energy from the expansion velocity reconstructed using the pump-probe experiments with the measured pump-alone ion kinetic energy. In order to extract the time dependent expansion velocity, the time resolved density in Fig. 6(b) is converted to nano-plasma radius using experimentally measured initial cluster size and the averaged ion charge (see appendix A for more technical details); the derivative of the radius is the expansion velocity shown in Fig. 7. The kinetic energy corresponding to the expansion velocity at the end of the detected range is 12.5 keV. The directly measured ion energy in the pump-alone case for the same experimental conditions (Fig. 4(e, green)) has 820 eV mean and 6.8 keV cutoff energy. Therefore, even the fastest detected ion in the pump-alone case is slower that the reconstructed averaged ion kinetic energy, when the resonance condition in pump-probe experiments is assumed to follow n_c in the SWIR range. Thus, the assumption of the resonance condition of n_c fails for probe wavelengths of $\gtrsim$1.4 μm.

DISCUSSION

When the simulated pump-probe scans are analyzed in exactly the same way as the experimental ones, an excellent agreement between them is observed (see red and green data points in Fig. 6(c)), validating the predictive power of MD

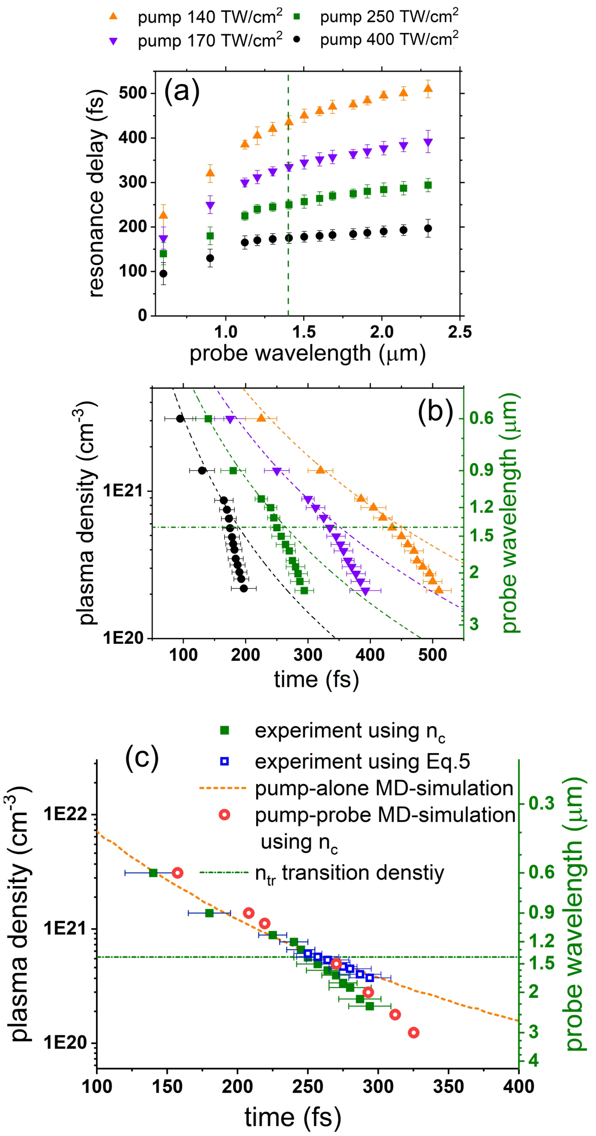

FIG. 6. **(a)** Experimentally measured dependence of the resonant delay on the probe wavelength for different pump intensities. **(b)** Corresponding reconstructed plasma density. The scatter-plots are experimental results; the dashed lines are pump-alone simulations. The reconstruction is based on the assumption that n_c is the resonance plasma density. **(c)** Nano-plasma density. **(green squares)**: reconstruction from the experimental data for 250 TW/cm^2 pump intensity, which is identical to (b, green squares). The n_c resonance condition is used. **(blue squares)**: same, but the resonance condition is defined by Eq. 5. **(red circles)**: MD simulation pump-probe results for 200 TW/cm^2 pump intensity reconstructed identically to the experimental data. **(orange dashed line)**: the dynamics of the averaged plasma density of the cluster after ionization by the pump pulse (without any probe pulse) calculated in MD-simulations. **(green dash-dotted line)**: horizontal line indicating transition density of $n_{tr} = 5.7 \times 10^{20}$ cm^{-3} and corresponding to the probe wavelength of 1.4 μm.

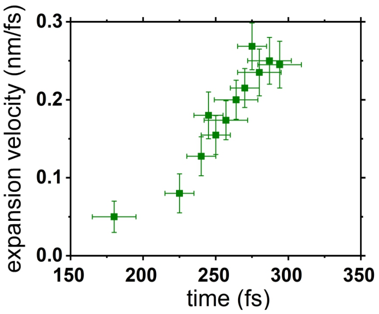

FIG. 7. Nano-plasma expansion velocity for the case of 250 TW/cm^2 pump intensity reconstructed from the density shown in Fig. 6(a,green).

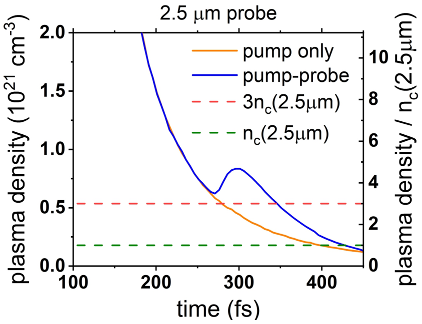

FIG. 8. MD-simulations of the temporal dependence of the nanoplasma density at 2.5 μm probe wavelength and the resonance pump-probe delay of 310 fs, which corresponds to the highest heating rate and the highest average ion kinetic energy. Simulation parameters: the pump pulse has 0.8 μm central wavelength, 60 fs FWHM pulse duration, and 200 TW/cm^2 peak intensity; the probe pulse has 100 TW/cm^2 intensity and 60 fs duration. Time zero is the peak of the pump pulse.

simulations. Note that the averaged density is used in the analysis, since the expanding nano-plasma from cluster ionization has radially inhomogeneous density [16, 37]. In addition, an alternative simulation approach based on a simpler nanoplasma (NP) model [7] doesn't reproduce the experimental results at SWIR wavelengths as can be seen in Appendix E. Thus, MD-simulations are essential for the interpretation of the experiments.

Fig. 5(a) and Fig. 8 present two examples of simulated dynamics of the nano-plasma density at the resonant pump-probe delay for a NIR wavelength of 0.9 μm, where n_c assumption is valid, and for a SWIR wavelength of 2.5 μm, where it fails. In the SWIR wavelength range the nanoplasma resonance shifts to densities higher than $n_c(\lambda_{probe})$ (for the pump-alone case and higher than $3n_c(\lambda_{probe})$ in the pump-probe scenario). As identified in MD simulations, the reason for this transition is the increase of the portion of electrons that are outer-ionized as shown in Fig. 9. An outer-ionized electron is an electron that left the cluster and caused a positive net charge in the remaining nano-plasma. This results in an increase of the Coulomb pressure contribution to the expansion force and reduces the importance of the thermal pressure. Since Coulomb pressure is inverse proportional to the fourth

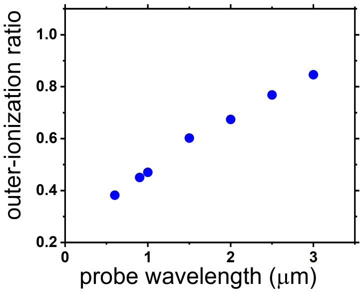

FIG. 9. Electron outer-ionization ratio at the resonant delay, which is the part of electrons left the plasma at the end of the interaction. Calculated from the same MD-simulation results as in Fig. 6(c, red circles).

power of the cluster radius (r): $P_c = Q^2/4\pi r^4$ [7] (Q is the total net charge), it favors smaller plasma sizes with higher density and occurs at shorter pump-probe delays. The increase of the portion of electrons that are outer-ionized at longer probe wavelengths is naturally expected from the fact that the nano-plasma size at the resonance delay is increasing and the Coulomb potential is inversely proportional to the plasma radius, such that the escape kinetic energy is $K_{esc} = eQ/r$. At the same time, the mean electron energy doesn't change significantly in the studied range (see Fig. 13 in the appendix).

A fit of the presented experimental results provides the following modified expression for the nano-plasma resonance condition:

$$\begin{aligned} n_{res}(\lambda) &= n_c(\lambda) \times \begin{cases} 1 & ,\lambda \leq 1.4 \\ 1 + (\lambda - 1.4) & ,\lambda > 1.4 \end{cases} \\ &= m_e \pi c^2/e^2 \times \begin{cases} 1/\lambda^2 & ,\lambda \leq 1.4 \\ (1 + \lambda - 1.4)/\lambda^2 & ,\lambda > 1.4 \end{cases} \end{aligned} \tag{5}$$

where λ is the probe wavelength in μm. Validity of this expression is experimentally proven up to 2.3 μm by the results presented here. When Eq. 5 is used for the reconstruction of the nano-plasma density from the pump-probe scans, a perfect agreement with the pump-alone case is obtained as presented in Fig. 6(c, blue).

Let's discuss why the observed transition happens at the plasma density of $n_{tr} = 5.7 \times 10^{20}$ cm^{-3}, which corresponds to the probe wavelength of ~1.4 μm (Fig. 6). A nano-plasma electron accelerated by the laser field has two main alternatives when contributing to laser absorption: (i) heat the plasma by elastic scattering on ions and other electrons or ionization of an ion in an inelastic process; (ii) leave the plasma and increase outer-ionization. The first scenario dominates under conditions when electrons have high probability of multiple scattering events as they traverse the nano-plasma. The second scenario prevails when scattering and collisional ionization rates drop below one per oscillation through the nano-plasma. The ionization (scattering) probability for an electron crossing the nano-plasma is $P = 2\sigma \int_0^\infty n_i(r)dr$, where σ is the ionization (scattering) cross section, $n_i(r)$ is the radially dependent ion density. In a simplified assumption of homogeneous plasma density, the expression is reduced to $P = 2\sigma n_i r = \sigma n_i d$, where d is the nano-plasma diameter. The ion density for the case of P=1 (the transition point with one scattering event) is $n_{i\,tr} = 1/d\sigma$, which is equivalent to the discussed condition of the electron mean free path (l) equal to the plasma diameter, since $l = 1/\sigma n_{i\,tr} = d$. From the preservation of the total number of ions we have $n_i r^3 = n_{i0} r_0^3$, where n_{i0} is the initial plasma density (which is equal to the ion density right after the pump pulse) and r_0 is the initial cluster radius, which is equal to the radius of the nano-plasma after the pump pulse. Thus $r = r_0 (n_{i0}/n_i)^{1/3}$ and $n_i(P=1) = (1/2 r_0 n_{i0}^{1/3} \sigma)^{3/2}$.

The total cross section for argon is about 8×10^{-16} cm^{-2} [38] at ~100 eV electron energy, which is a typical electron energy scale at the peak of the probe pulse as identified in MD-simulations. The corresponding estimate of the transition ion density is $n_i = 2 \times 10^{20}$ cm^{-3} (for the experimentally measured r_0=7 nm), which is equivalent to the transition plasma density of 5×10^{20} cm^{-3} taking into account the experimentally measured averaged ion charge state of 2.5 (for the pump-alone scenario and the analyzed intensity of 250 TW/cm^2). This estimate is in a good agreement with the measured transition density. Thus, the observed transition in the nature of the nano-plasma response happens when the electron mean free path becomes larger than the nano-plasma diameter and equivalently the probability of the electron interaction with the nano-plasma drops below unity.

CONCLUSIONS

In conclusion, we have experimentally identified that the resonant nano-plasma density in the SWIR range differ from the critical plasma density, which defines the resonance condition in the visible and NIR ranges. These findings are enabled by the extension of the laser-nano-plasma experiments into the SWIR range. With the help of molecular dynamics simulations, we found that the observed effect is attributed to the reduction of the electron scattering rate and corresponding heating as the plasma gets more dilute and, at the same time, the increased portion of electrons that are outer-ionized. It corresponds to a transition from a thermal pressure dominant expansion to a Coulomb pressure dominant conditions. Based on the experimental results and MD-simulations, which are in almost perfect agreement, we derived a modified nano-plasma resonant density, which is valid (at the very least) from visible to SWIR spectral ranges. These findings are important for a broad range of applications, as they are relevant for plasma physics at surfaces such as ion acceleration, coherent X-ray generation via oscillating relativistic plasma mirrors, and pulse cleaning with plasma mirrors.

The work was supported by US Air Force Office of Scientific Research under award number FA-9550-15-1-0037 and FA-9550-21-10415.

The authors thank Zhou Wang and Hyunwook Park for useful discussions.

DATA AVAILABILITY STATEMENT

The data that support the findings of this study are available from the corresponding author upon reasonable request.

Appendix A. Dependence of pump-probe and pump-alone results on the pump intensity

In this section, we discuss the dependence of the results on the intensity of the pump beam, while all other experimental conditions are the same as in the main text.

Fig. 10(a) presents measured ion spectra for different pump intensities for the pump-alone case. These spectra were used to calculate the average ion kinetic energy and the corresponding average ion velocity (taking into account the mass of an argon ion). The extracted velocity is shown in Fig. 10(b). This velocity should be directly related to the pump-probe delay at later expansion stages (which is equivalent to a longer probe wavelength) when plasma pressure and acceleration become negligible. Thus, we could take a probe wavelength from the red end of the tuning range and measure the dependence of the resonance delay on the pump intensity. The result in presented in Fig. 10(c).

Let's estimate the expected relation between the expansion velocity and the pump-probe resonance delay. The density (n) of an expending spherically symmetrical plasma at time t is:

$$n(t) = n(t=0)\left(\frac{r(0)}{r(t)}\right)^3, \tag{6}$$

where r is the plasma radius. This equation is derived in the assumption of a homogeneous plasma with a sharp edge; in practice, nano-plasma has density gradient, so n and r should be treated as radially averaged density and radius.

Taking into account that the relation between the radial expansion velocity (v_{exp}) and the nano-plasma radius ($\mathrm{v}_{exp} = \dot{r}$), Eq. 6 becomes:

$$n(t) = n(t=0)\left(\frac{r(0)}{r(0)+\int_0^t \mathrm{v}_{exp}(t')dt'}\right)^3. \tag{7}$$

In the simplified assumption of constant expansion velocity, we get:

$$n(t) = n(t=0)\left(\frac{r(0)}{r(0)+\mathrm{v}_{exp}t}\right)^3. \tag{8}$$

Resonance happens when the nano-plasma density reaches the resonance density for a given probe frequency (ω_{probe}) $n(t=t_{res}) = n_{res}(\omega_{probe})$, where Eq. 5 should be used for the resonance conditions. Thus, the expression for the resonance delay is:

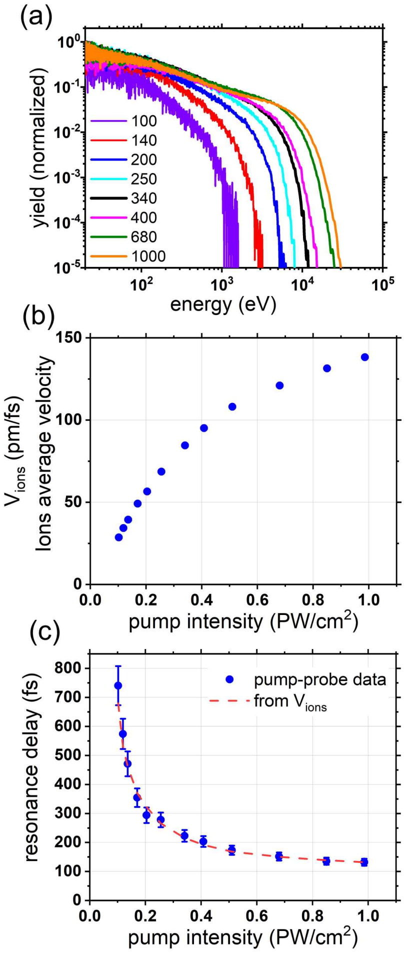

FIG. 10. **(a)** Measured ion spectra for different pump (800 nm) intensities (pump-alone case). The legend indicates intensity in TW/cm^2. **(b)** Final stationary plasma expansion velocity defined as ions averaged velocity calculated from the data in (a). **(c)** (blue dots) Experimental pump-probe results. Resonance delay dependence on pump intensity for the fixed probe wavelength of 1.9 µm. (red line) The resonance delay reconstructed from the data in (b) using Eq. 9.

$$\tau(n = n_{res}(\omega_{probe})) = \frac{r(0)}{\mathrm{v}_{exp}}\left(\left(\frac{n(t=0)}{n_{res}(\omega_{probe})}\right)^{\frac{1}{3}} - 1\right). \tag{9}$$

Therefore, the resonance delay is inverse proportional to the expansion velocity for a fixed probe wavelength. Indeed, if we calculate the expected resonance delay using Eq. 9 and the measured expansion velocity, we get almost perfect agreement with the pump-probe results (see red line in Fig. 10(c)). Here the measured cluster size of 7 nm was used. $n(0)$ was estimated by measuring the averaged ions charge and multiplying it by the initial argon density of 1.8×10^{22} cm^{-3}. The ion charge was measured in the mass-spectrometer mode by applying an accelerating potential of 2 kV to the interaction region, which was done with a pair of field plates: one quar-

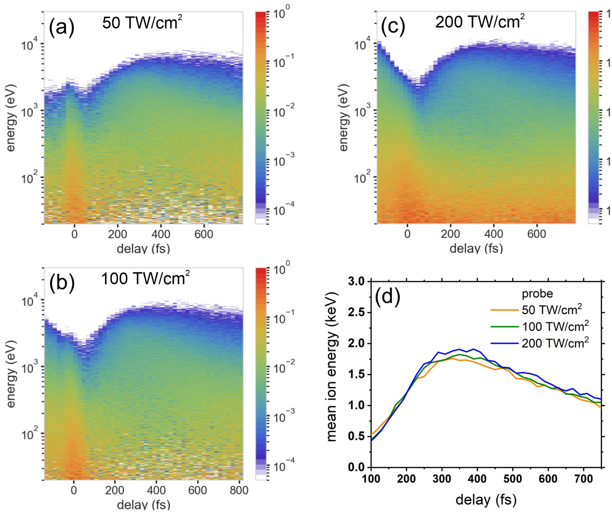

FIG. 11. Test of the influence of the probe intensity on the measurement. As an example the data for 1900 nm probe pulse is shown for the peak intensity of 50 TW/cm^2 **(a)**; 100 TW/cm^2 **(b)**; 200 TW/cm^2 **(c)**. In all cases the 800 nm-pump intensity is 140 TW/cm^2, and the cluster beam is identical to the results in the paper (Ar, 30 bar backing pressure). **(d)** Ion mean energy slice for all three cases provides identical resonance delay within the experimental uncertainty: 348 ± 20 fs for 50 TW/cm^2; 345 ± 20 fs for 100 TW/cm^2; 344 ± 20 fs for 200 TW/cm^2.

ter inch above and another quarter inch below the interaction region. The perfect agreement serves as an additional confirmation of the correctness of the measured cluster size of 7 nm.

Appendix B. Proof of the resonance delay tolerance to the probe intensity

Particular care was taken to exclude any systematic influence of the probe pulse parameters on the experimental results. We experimentally tested that the probe intensity used in the experiments (which was in the range 80-100 TW/cm^2) do not affect the experimental results. In order to demonstrate it, a series of pump-probe scans with different probe intensity but fixed pump and cluster parameters was taken. As can be seen in Fig. 11, twice higher and twice lower intensity of the probe pulse results in the same resonance delay. Note that the results presented here are for the pump intensity of 140 TW/cm^2, which is lower than in the main discussed result presented in Fig. 6(e). It is to exaggerate the effect, as the intensity of the probe pulse should have a more pronounced effect for lower pump intensities when they start to approach each other. Thus, the probe intensity used in the experiments do not affect the resonance position in the pump-probe scans.

Pulse duration was found to have a small effect on the result and, to exclude it, the pulse duration was kept constant (50 fs ± 10 fs; Fig. 12) over the whole wavelength scanning range. The pulse duration of 800 nm pulse was also in the same range, namely 60 fs as measured with SHG-FROG.

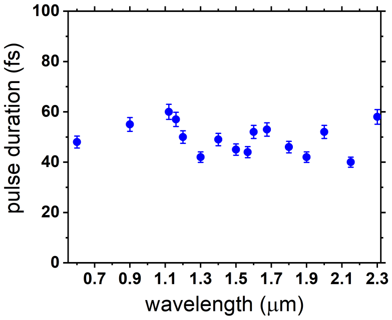

FIG. 12. On-target duration of probe pulses measured with a SHG-FROG setup.

Appendix C. Estimation of the dependence of the outer-ionization yield on the probe wavelength

As discussed in the main text, it is expected that the portion of outer-ionized electrons will increase for longer wavelengths because the Coulomb potential of the ion cloud and the corresponding escape electron energy $K_{esc} = eQ/r$ (Q is the total positive net charge, e is the electron charge, r is the nano-plasma radius) are decreasing for larger cluster sizes and correspondingly for longer wavelengths that have resonance at later expansion times. In the following, we present an estimate of outer-ionization rate.

The first important note is that the electron energy distribution at the resonance delay follow thermal Maxwell–Boltzmann distribution (Fig. 13(a)) with mean electron energy of about 240 eV for all studied probe wavelengths (for the same conditions as everywhere in the paper: 800 nm, 60 fs pump with 200 TW/cm^2, argon clusters with 2 nm radius). At the same time, the electron escape energy is decreasing with time, as the plasma radius and the corresponding resonance probe wavelength are increasing as shown in Fig. 13(b) (the nano-plasma radius is obtained from MD simulations as the distance between the center of the cluster to the furthest ion).

Electron energy distribution can be expressed as $f(K,K_0,N_0) = N_0/K_0 \times exp(-K/K_0)$, where K is the kinetic energy, K_0 is the mean kinetic energy (equal to the electron temperature of the plasma), N_0 is the total number of electrons. If there is an escape potential barrier of K_{esc}, so that there is more than one electron above this barrier, these electrons will escape plasma, which will experience evaporation cooling. The electrons remaining after removing particles with $K > K_{esc}$ will thermalize and approach exponential energy distribution with smaller mean kinetic energy. In a simplified static scenario when the plasma expansion and ionization is neglected, the cooling process stops when the final electron temperature (K_f) drops to the level when there are no electrons above K_{esc} (or strictly speaking $f(K_{esc},K_f,N_f) < 1$, where N_f is the number of electrons left in plasma at the end of the cooling process). The final election energy distribution

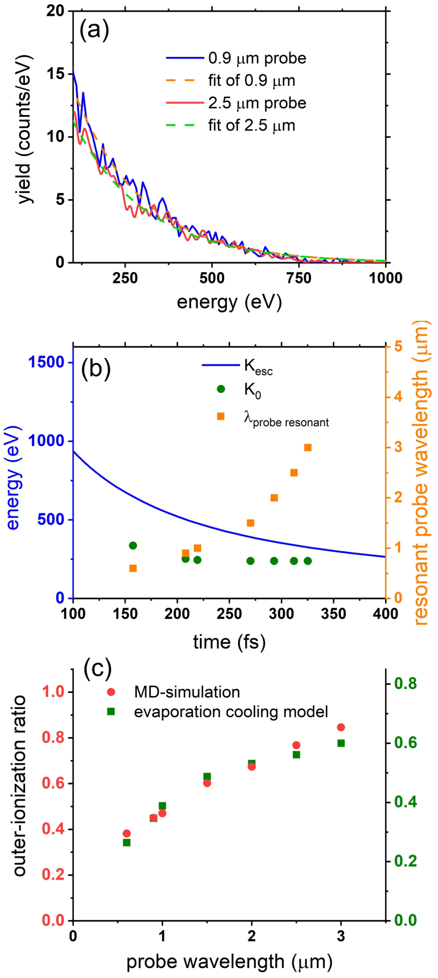

FIG. 13. **(a)** The electron energy distribution at the peak of the probe pulse for the case of the resonance pump-probe delay. $f(K,K_0,N_0) = N_0/K_0 \times exp(-K/K_0)$ fit function is used to plot dashed lines, which show that the electron energy distribution follow the thermal energy distribution, and the result is similar for all wavelength in the studied range. **(b)** The electron escape energy (blue line) and the mean kinetic energy (green circles) at different probe wavelengths. **(c)** The electron outer-ionization ratio (the portion of electrons that are outer-ionized). Red scatters present the result of the MD simulation, green scatters are the estimate based on the presented here (simplified compared to MD simulations) evaporation cooling model.

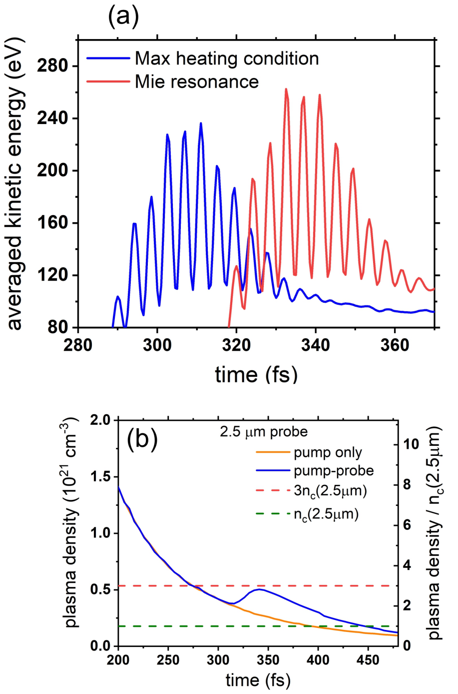

FIG. 14. **(a)** Averaged (over ensemble) kinetic energy of plasma electrons for the maximum heating condition (blue) according to the modified resonance density and the standard resonance condition (red). The pump is the same as in all other simulations: 800 nm pulse with 2×10^{14} W/cm^2 and 60 fs duration. The case of 2500 nm probe is presented (60 fs pulse duration and 1×10^{14} W/cm^2 peak intensity). Although the maximum final energy of ions and electrons and the corresponding optimum laser absorption condition is observed at 310 fs delay (blue line); the maximum electron kinetic energy during the probe pulse is observed at the standard resonance conditions at 340 fs delay (red line). Time zero is the peak of the pump pulse. **(b)** Temporal dependence of the nano-plasma density for the standard resonance case for 2500 nm probe (340 fs pump-probe delay). The maximum heating case is shown in Fig. 8.

can ba expressed as $f(K,K_f) = N_0/K_0 \times exp(-K/K_f)$ (the normalization in front of the exponent is preserves as nothing happens with very slow electrons during the cooling process, in the first approximation). Thus, the number of electrons left in the plasma after the evaporation cooling is $N_f = \int f(K,K_f) = N_0K_f/K_0$, and K_f is determined by $\int_{K_{esc}}^{\infty} f(K,K_f) = N_0/K_0 \times exp(-K_{esc}/K_f) = 1$. Then, $K_f = K_{esc}/log(N_0/K_0)$. Therefore, $N_f = N_0K_{esc}/K_0log(N_0/K_0)$, and the portion of the outer-ionized electrons is $P_{outerionized} = (N_0 - N_f)/N_0 = 1 - K_{esc}/K_0log(N_0/K_0)$ (note that the expression is assuming that there is at least some outer-ionization and $K_{esc}/K_0log(N_0/K_0) \leq 1$). The calculated $P_{outerionized}$ using data from the MD-simulations is shown in Fig. 13(c). The trend clearly follows the result of MD-simulations, although there is an offset in absolute values that should be caused by simplifications made in the model: ignoring electron impact ionization, plasma expansion, and dynamical change of the escape potential (while the nano-plasma net charge is increasing)

Appendix D. Maximum instantaneous electron energy (MD-simulations)

As discussed in the main text, the resonance condition for the maximum final ion kinetic energy is shifting to higher than n_c plasma density at mid-IR probe wavelengths according to Eq. 5. However, it is worth mentioning that the standard resonance condition of n_c still corresponds to the maximum instantaneous electron kinetic energy as shown in Fig. 14. The reason is already discussed in the main text, and it is the drop

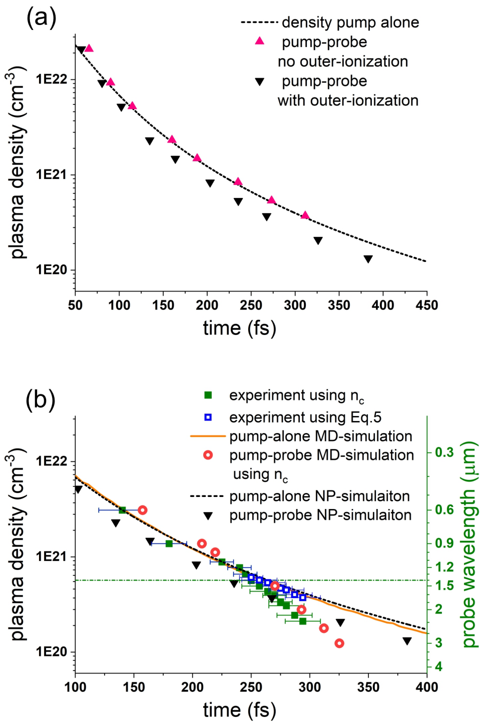

FIG. 15. **(a)** Plasma density in NP-simulations. (scatters): pump-probe results. Reconstruction is similar to experiments and MD-simulations, but the standard Mie resonance condition of $3n_c$ is used, as it is the part of the model. (black dashed line): NP-model pump-alone result. **(b)** Comparison of NP-model results to MD-simulations and experiment. The pump-alone density is similar to the MD-simulation output, but the pump-probe result in the NP-model do not reproduce the experiment. Note that the nanoplasma model doesn't reproduce correctly the intensity scaling, so the intensity in simulations was tuned to approximately match the experimental data.

of the electron scattering rate below one per crossing the nanoplasma. Thus, the higher instantaneous electron kinetic energy is not transferred into stronger laser absorption because the laser energy can be absorbed only during scattering events, while free electrons can't absorb.

Appendix E. Pump-probe simulation in the nanoplasma model [7].

A code based on the nanoplasma (NP) model was written to compare its results the experimental results and MD-simulations. The NP-model results are presented in Fig. 15. The code is mostly based on equations from the original NP-model paper [7] with small upgrades from later papers [39]. It was tested to reproduce results from the previous NP-model papers.

As seen in Fig. 15 and already mentioned in the main text, NP-model fails to reproduce the experimental results in the mid-IR range. However, it gets the right direction of the shift of the pump-probe results relative to the pump-alone density (see Fig. 15). In addition, if we turn off the electron outer-ionization in the NP-model, pump-probe result perfectly agrees with the pump-alone density, which provides an additional support for the crucial importance of the outer-ionization for the observed effect and conclusions in the main text.

Note that in the NP-model pump-probe reconstruction the resonance condition is $3n_c$ (unlike n_c in the MD-model) due to the homogeneous density assumption and the corresponding equations used in the NP-model.

---

* leshchenko.1@osu.edu

[1] M. C. Downer, R. Zgadzaj, A. Debus, U. Schramm, and M. C. Kaluza, Diagnostics for plasma-based electron accelerators, Rev. Mod. Phys. **90**, 035002 (2018).

[2] A. B. Zylstra *et al.*, Burning plasma achieved in inertial fusion, Nature **601**, 542 (2022).

[3] H.-J. Kunze, Plasma diagnostics, in *Plasma Physics: Confinement, Transport and Collective Effects*, edited by A. Dinklage, T. Klinger, G. Marx, and L. Schweikhard (Springer Berlin Heidelberg, Berlin, Heidelberg, 2005) pp. 349–373.

[4] A. Donné, Introduction to plasma diagnostics, Fusion Science and Technology **45**, 383 (2004).

[5] K. K. Ostrikov, F. Beg, and A. Ng, Colloquium: Nanoplasmas generated by intense radiation, Rev. Mod. Phys. **88**, 011001 (2016).

[6] H. M. Milchberg, S. J. McNaught, and E. Parra, Plasma hydrodynamics of the intense laser-cluster interaction, Phys. Rev. E **64**, 056402 (2001).

[7] T. Ditmire, T. Donnelly, A. M. Rubenchik, R. W. Falcone, and M. D. Perry, Interaction of intense laser pulses with atomic clusters, Phys. Rev. A **53**, 3379 (1996).

[8] K. Y. Kim, I. Alexeev, E. Parra, and H. M. Milchberg, Time-resolved explosion of intense-laser-heated clusters, Phys. Rev. Lett. **90**, 023401 (2003).

[9] T. Döppner, T. Fennel, P. Radcliffe, J. Tiggesbäumker, and K.-H. Meiwes-Broer, Ion and electron emission from silver nanoparticles in intense laser fields, Phys. Rev. A **73**, 031202 (2006).

[10] S. Zamith, T. Martchenko, Y. Ni, S. A. Aseyev, H. G. Muller, and M. J. J. Vrakking, Control of the production of highly charged ions in femtosecond-laser cluster fragmentation, Phys. Rev. A **70**, 011201 (2004).

[11] S. R. Krishnan, C. Peltz, L. Fechner, V. Sharma, M. Kremer, B. Fischer, N. Camus, T. Pfeifer, J. Jha, M. Krishnamurthy, C.-D. Schröter, J. Ullrich, F. Stienkemeier, R. Moshammer, T. Fennel, and M. Mudrich, Evolution of dopant-induced helium nanoplasmas, New Journal of Physics **14**, 075016 (2012).

[12] J. Zweiback, T. Ditmire, and M. D. Perry, Femtosecond time-resolved studies of the dynamics of noble-gas cluster explosions, Phys. Rev. A **59**, R3166 (1999).

[13] D. D. Hickstein, F. Dollar, J. A. Gaffney, M. E. Foord, G. M. Petrov, B. B. Palm, K. E. Keister, J. L. Ellis, C. Ding, S. B. Libby, J. L. Jimenez, H. C. Kapteyn, M. M. Murnane, and W. Xiong, Observation and control of shock waves in individual nanoplasmas, Phys. Rev. Lett. **112**, 115004 (2014).

[14] T. Fennel, T. Döppner, J. Passig, C. Schaal, J. Tiggesbäumker, and K.-H. Meiwes-Broer, Plasmon-enhanced electron accelera-

tion in intense laser metal-cluster interactions, Phys. Rev. Lett. **98**, 143401 (2007).

[15] T. Gorkhover, S. Schorb, R. Coffee, M. Adolph, L. Foucar, D. Rupp, A. Aquila, J. D. Bozek, S. W. Epp, B. Erk, L. Gumprecht, L. Holmegaard, A. Hartmann, R. Hartmann, G. Hauser, P. Holl, A. Hömke, P. Johnsson, N. Kimmel, K.-U. Kühnel, M. Messerschmidt, C. Reich, A. Rouzée, B. Rudek, C. Schmidt, J. Schulz, H. Soltau, S. Stern, G. Weidenspointner, B. White, J. Küpper, L. Strüder, I. Schlichting, J. Ullrich, D. Rolles, A. Rudenko, T. Möller, and C. Bostedt, Femtosecond and nanometre visualization of structural dynamics in superheated nanoparticles, Nature Photonics **10**, 93 (2016).

[16] T. Nishiyama, Y. Kumagai, A. Niozu, H. Fukuzawa, K. Motomura, M. Bucher, Y. Ito, T. Takanashi, K. Asa, Y. Sato, D. You, Y. Li, T. Ono, E. Kukk, C. Miron, L. Neagu, C. Callegari, M. Di Fraia, G. Rossi, D. E. Galli, T. Pincelli, A. Colombo, T. Kameshima, Y. Joti, T. Hatsui, S. Owada, T. Katayama, T. Togashi, K. Tono, M. Yabashi, K. Matsuda, C. Bostedt, K. Nagaya, and K. Ueda, Ultrafast structural dynamics of nanoparticles in intense laser fields, Phys. Rev. Lett. **123**, 123201 (2019).

[17] I. V. Pogorelsky, M. N. Polyanskiy, and W. D. Kimura, Mid-infrared lasers for energy frontier plasma accelerators, Phys. Rev. Accel. Beams **19**, 091001 (2016).

[18] D. Woodbury, L. Feder, V. Shumakova, C. Gollner, R. Schwartz, B. Miao, F. Salehi, A. Korolov, A. Pugžlys, A. Baltuška, and H. M. Milchberg, Laser wakefield acceleration with mid-ir laser pulses, Opt. Lett. **43**, 1131 (2018).

[19] P. Kumar, K. Yu, R. Zgadzaj, M. Downer, I. Petrushina, R. Samulyak, V. Litvinenko, and N. Vafaei-Najafabadi, Evolution of the self-injection process in long wavelength infrared laser driven lwfa, Physics of Plasmas **28**, 013102 (2021), https://doi.org/10.1063/5.0027167.

[20] Z. Chang, L. Fang, V. Fedorov, C. Geiger, S. Ghimire, C. Heide, N. Ishii, J. Itatani, C. Joshi, Y. Kobayashi, P. Kumar, A. Marra, S. Mirov, I. Petrushina, M. Polyanskiy, D. A. Reis, S. Tochitsky, S. Vasilyev, L. Wang, Y. Wu, and F. Zhou, Intense infrared lasers for strong-field science, Adv. Opt. Photon. **14**, 652 (2022).

[21] G. D. Tsakiris, K. Eidmann, J. M. ter Vehn, and F. Krausz, Route to intense single attosecond pulses, New Journal of Physics **8**, 19 (2006).

[22] A. Gonoskov, Theory of relativistic radiation reflection from plasmas, Physics of Plasmas **25**, 013108 (2018).

[23] H. Daido, M. Nishiuchi, and A. S. Pirozhkov, Review of laser-driven ion sources and their applications, Reports on Progress in Physics **75**, 056401 (2012).

[24] T. Fennel, K.-H. Meiwes-Broer, J. Tiggesbäumker, P.-G. Reinhard, P. M. Dinh, and E. Suraud, Laser-driven nonlinear cluster dynamics, Rev. Mod. Phys. **82**, 1793 (2010).

[25] U. Saalmann, C. Siedschlag, and J. M. Rost, Mechanisms of cluster ionization in strong laser pulses, Journal of Physics B: Atomic, Molecular and Optical Physics **39**, R39 (2006).

[26] E. Esarey, C. B. Schroeder, and W. P. Leemans, Physics of laser-driven plasma-based electron accelerators, Rev. Mod. Phys. **81**, 1229 (2009).

[27] A. Macchi, M. Borghesi, and M. Passoni, Ion acceleration by superintense laser-plasma interaction, Rev. Mod. Phys. **85**, 751 (2013).

[28] C. Thaury, F. Quéré, J.-P. Geindre, A. Levy, T. Ceccotti, P. Monot, M. Bougeard, F. Réau, P. D'Oliveira, P. Audebert, R. Marjoribanks, and P. Martin, Plasma mirrors for ultrahigh-intensity optics, Nature Physics **3**, 424 (2007).

[29] U. Even, Pulsed Supersonic Beams from High Pressure Source: Simulation Results and Experimental Measurements, Advances in Chemistry **2014**, 636042 (2014).

[30] K. Y. Kim, V. Kumarappan, and H. M. Milchberg, Measurement of the average size and density of clusters in a gas jet, Applied Physics Letters **83**, 3210 (2003).

[31] Y. Tao, R. Hagmeijer, E. T. A. van der Weide, H. M. J. Bastiaens, and K.-J. Boller, Revisiting argon cluster formation in a planar gas jet for high-intensity laser matter interaction, Journal of Applied Physics **119**, 164901 (2016), https://doi.org/10.1063/1.4947187.

[32] V. S. Popov, Tunnel and multiphoton ionization of atoms and ions in a strong laser field (keldysh theory), Physics-Uspekhi **47**, 855 (2004).

[33] F. Grasbon, G. G. Paulus, H. Walther, P. Villoresi, G. Sansone, S. Stagira, M. Nisoli, and S. De Silvestri, Above-threshold ionization at the few-cycle limit, Phys. Rev. Lett. **91**, 173003 (2003).

[34] U. Saalmann, Cluster nanoplasmas in strong FLASH pulses: formation, excitation and relaxation, Journal of Physics B: Atomic, Molecular and Optical Physics **43**, 194012 (2010).

[35] Z. Wang, A. Camacho Garibay, H. Park, U. Saalmann, P. Agostini, J. M. Rost, and L. F. DiMauro, Universal high-energy photoelectron emission from nanoclusters beyond the atomic limit, Phys. Rev. Lett. **124**, 173201 (2020).

[36] V. Krainov and M. Smirnov, Cluster beams in the super-intense femtosecond laser pulse, Physics Reports **370**, 237 (2002).

[37] C. Peltz, J. A. Powell, P. Rupp, A. Summers, T. Gorkhover, M. Gallei, I. Halfpap, E. Antonsson, B. Langer, C. Trallero-Herrero, C. Graf, D. Ray, Q. Liu, T. Osipov, M. Bucher, K. Ferguson, S. Möller, S. Zherebtsov, D. Rolles, E. Rühl, G. Coslovich, R. N. Coffee, C. Bostedt, A. Rudenko, M. F. Kling, and T. Fennel, Few-femtosecond resolved imaging of laser-driven nanoplasma expansion, New Journal of Physics **24**, 043024 (2022).

[38] M. Inokuti, Introduction, total scattering cross sections, elastic scattering cross section, excitation: Datasheet from landolt-börnstein - group i elementary particles, nuclei and atoms · volume 17a: "interactions of photons and electrons with atoms" in springermaterials (https://doi.org/10.1007/10547143_2), copyright 2000 Springer-Verlag Berlin Heidelberg.

[39] S. Micheau, H. Jouin, and B. Pons, Modified nanoplasma model for laser-cluster interaction, Phys. Rev. A **77**, 053201 (2008).